International Journal of Extreme Manufacturing

Designing electrolyte with multi-ether solvation structure enabling low-temperature sodium ion capacitor

OPEN ACCESS
IMMT | IOP Publishing
International Journal of Extreme Manufacturing
Int. J. Extrem. Manuf. 7 (2025) 045504 (10pp)
https://doi.org/10.1088/2631-7990/adbfe0

Designing electrolyte with multi-ether solvation structure enabling low-temperature sodium ion capacitor

Dongming Liu[1], Mengfan Pei[1], Xin Jin[1], Lin Wang[2], Wanyuan Jiang[2], Borui Li[1], Runyue Mao[1], Xigao Jian[1,2] and Fangyuan Hu[1,*]

[1] School of Materials Science and Engineering, State Key Laboratory of Fine Chemicals, Frontiers Science Center for Smart Materials Oriented Chemical Engineering, Technology Innovation Center of High-Performance Resin Materials (Liaoning Province), Dalian University of Technology, Dalian 116024, People's Republic of China
[2] State Key Laboratory of Fine Chemicals, Frontiers Science Center for Smart Materials Oriented Chemical Engineering, School of Chemical Engineering, Technology Innovation Center of High-Performance Resin Materials (Liaoning Province), Dalian University of Technology, Dalian 116024, People's Republic of China

E-mail: hufangyuan@dlut.edu.cn

Received 10 July 2024, revised 23 December 2024
Accepted for publication 12 March 2025
Published 4 April 2025

Abstract

Sodium-ion hybrid capacitors (SICs), which combine the high energy density of batteries with the high power density and long cycle life of capacitors, are considered promising next-generation energy storage devices. Ensuring the performance of SICs in low-temperature environments is crucial for applications in high-altitude cold regions, where the desolvation process of Na^+ and the transport process in the solid electrolyte interphase (SEI) are determinant. In this paper, we proposed a multi-ether modulation strategy to construct a solvation sheath with multi-ether participation by modulating the coordination of Na^+ and solvents. This unique solvation sheath not only reduces the desolvation energy barrier of Na^+, but more importantly forms a Na_2O-rich inorganic SEI and enhances the ionic dynamics of Na^+. Benefiting from the excellent solvation structure design, SICs prepared with this electrolyte can achieve energy density of up to 178 $Wh{\cdot}kg^{-1}$ and ultra-high power density of 42 390 $W{\cdot}kg^{-1}$ at room temperature. Notably, this SIC delivers record-high energy densities of 149 $Wh{\cdot}kg^{-1}$ and 119 $Wh{\cdot}kg^{-1}$ as well as power densities of up to 25 200 $W{\cdot}kg^{-1}$ and 24 591 $W{\cdot}kg^{-1}$ at −20 °C and −40 °C, respectively. This work provides new ideas for the development of high-performance SICs for low-temperature operating environments.

Supplementary material for this article is available online

Keywords: sodium ion capacitors, solvated structure, Na_2O-rich SEI, low operating temperature

* Author to whom any correspondence should be addressed.

1. Introduction

Hybrid ion capacitors are considered a promising energy storage device by combining a battery-type negative electrode and a capacitor-type positive electrode, which significantly improves energy density while providing high power density and long cycle life[1–4]. Currently, lithium-ion capacitors have been successfully commercialized. However, the shortage of lithium resources and high cost limit the further development of lithium-ion capacitors. Compared to lithium-ion capacitors, sodium-ion capacitors have lower costs, while the smaller Stokes radius gives sodium-ion capacitors an advantage in low-temperature operating environments[5–7]. Unfortunately, however, the scarcity of operational data for sodium-ion capacitors in low-temperature operating environments severely restricts their deployment in some high-altitude regions and extremely cold climates. Therefore, it is necessary to further explore the low-temperature performance of sodium-ion capacitors.

Sodium ion capacitors (SICs) typically consist of a battery-type hard carbon anode and a capacitance-type activated carbon cathode, together with ester-based (e.g., EC/DEC) or ether-based (e.g., DME) electrolyte[8,9]. Due to the typical battery characteristics of the hard carbon anode, the slow ionic dynamics on the anode side significantly affect the electrochemical performance of the SIC[10–12]. Sodium ions inserted into hard carbon undergo four steps. In a typical charging process with $NaPF_6$ in EC/DEC (1: 1) electrolyte, for example, 1) solvated Na^+ moves toward the anode in the electrolyte under potential, 2) Na^+ desolvates at the electrode/electrolyte interface, 3) desolvated Na^+ passes through the solid electrolyte interface (SEI), and 4) Na^+ is inserted into the body phase of the hard carbon anode[13,14]. Notably, the desolvation process of Na^+ and the transport process of Na^+ in the SEI are considered to significantly affect the ionic dynamics of Na^+ at low-temperature operating environments[15]. The desolvation process of Na^+ in low-temperature operating environments is closely related to the polar of solvent selected and the solvation sheath formed by the selected solvent and Na^+[16]. For example, the Na^+ solvating sheath in commercial ester-based electrolytes consists mainly of highly polar carbonate molecules. The strong coordination of carbonate molecules with Na^+ is unfavorable for Na^+ transport and desolvation in low-temperature operating environments[17]. In addition, highly polar solvent molecules tend to have higher melting points, causing the electrolyte to solidify in low-temperature working environments[18]. Replacing the carbonate with a low-polarity solvent (e.g., an ether solvent) can reduce the binding energy between Na^+ and the solvent, making Na^+ easier to desolvate[19–21]. Unfortunately, however, the weak polarity of the ether-based molecules and their weak coordination with Na^+ easily lead to the precipitation of sodium salts (e.g., $NaPF_6$) and the solidification of the electrolyte at temperatures higher than the freezing point in low-temperature environments. At present, the vast majority of ether-based electrolytes still have relatively low ionic conductivity in low-temperature environments, which could not satisfy the operational requirements in low-temperature environments. It is necessary to prepare ether-based electrolytes with high ionic conductivity in low-temperature environments through rational electrolyte chemistry.

The composition of the SEI on the anode surface also influences the ionic transport of Na^+ in the low-temperature operating environment[22]. It is worth noting that the composition of the SEI is also closely related to the Na^+ solvation structure[23]. Previous work has shown that SEIs composed of unstable organic sodium salts and sodium carbonate lead to degradation of anode performance[24]. The general strategy is to reduce the amount of solvent in the Na^+ solvation sheath by using a lower polarity solvent, so that more anions are involved in the solvation sheath structure, and the solvent-dominated solvation structure is gradually transformed into an anion-dominated solvation structure[25,26]. The anions are reduced at the anode surface, forming an anion-derived inorganic SEI (e.g., NaF). The anion-derived NaF-based SEI is usually considered to be favorable for fast Na^+ transport[27]. However, recent studies in lithium-ion batteries have shown that LiF has lower ionic conductivity and higher diffusion energy barriers for lithium ions compared with other inorganic lithium salt[28,29]. Among them, Li_2O has been proven to have lower ionic diffusion energy barriers and higher ionic conductivity. The ionic dynamics of Li^+ can be significantly enhanced by constructing Li_2O-dominated SEIs[30,31]. This provides a good inspiration for Na^+ transport in low-temperature operating environments. Unfortunately, however, there are no relevant reports on Na_2O-rich SEIs. It is an attractive strategy to enhance the ionic dynamics of Na^+ in low-temperature operating environments by modulating the Na^+ solvation sheath structure to reduce the desolvation energy of Na^+ while constructing a Na_2O-rich SEI.

Here, we propose a rational solvation modulation strategy to modulate the solvent structure of the solvated sheath by using ether-based solvents containing different numbers of ether bonds (THF, DME, and DIG). Multiple solvents involved in the solvation sheath decreased the desolvation energy of Na^+. More importantly, the Na_2O-rich inorganic SEI derived from this unique solvated structure ensures rapid Na^+ transport in the SEI and enhances the ionic kinetics of Na^+ in low-temperature operating environments. Benefiting from the fast Na^+ ionic kinetics, the HC anode achieves a specific capacity of 331 $mAh{\cdot}g^{-1}$ at 0.05 $A{\cdot}g^{-1}$ current density at −40 °C, and maintains a specific capacity of 200 $mAh{\cdot}g^{-1}$ even at 2 $A{\cdot}g^{-1}$. SICs constructed with hard carbon (HC) and activated carbon (AC) have energy densities of up to 178 $Wh{\cdot}kg^{-1}$ and power densities of up to 42 390 $Wh{\cdot}kg^{-1}$ in a room-temperature operating environment. Energy densities of up to 149 $Wh{\cdot}kg^{-1}$ and 119 $Wh{\cdot}kg^{-1}$ were achieved at temperatures of −20 °C and −40 °C. To our knowledge, these are the highest values achieved to date for SICs in low-temperature operating

environments. These impressive performances provide new insights into the design of SICs for low-temperature operating environments.

2. Results and discussion

The solvated structure of Na^+ has a great influence on the performance of SICs. We expect to construct a Na^+ solvation sheath formed by a variety of low-polarity ether-based solvents to improve the solvation behavior of Na^+. At the same time, through modulation of the Na^+ solvation structure, we successfully optimized the solid electrolyte interphase (SEI) composition, thereby achieving a 'dual-acceleration' effect on Na^+ transport kinetics, as evidenced in Figures 1(a) and (b). After careful selection, we chose the solvents THF, DME, and DIG containing 1, 2, and 3 numbers of ether groups, respectively. THF, DME, and DIG have similar dielectric constants (ε) and donor numbers (DN) (Table S1). This ensures that they have similar solvation behavior in the electrolyte. To involve each solvent in the solvation sheath, we formulated the 1 M $NaPF_6$ in THF/DME/DIG (1: 1: 1 vol%) electrolyte, abbreviated as TE, by mixing these solvents in equal proportions. To ensure that the electrolyte has a high ionic conductivity, it is necessary to first make sure that the electrolyte stays in the liquid state under a low-temperature operating environment. Among several electrolytes composed of different solvents, 1 M $NaPF_6$ in TE remained liquid at −60 °C, while single-ether electrolytes (1 M $NaPF_6$ in THF, DME, and DIG, denoted as NaT, NaD, and NaG, respectively) and 1 M $NaPF_6$ in EC/DEC electrolyte underwent coagulation, as shown in Figures 1(c) and (d). This is due to the increase in solvent type elevates the entropy of the electrolyte system and lowers the crystallization point of the electrolyte[32]. DSC test shows similar results (Figure S1). Compared to single-ether electrolytes, the crystallization point of TE electrolytes can reach up to −76 °C, which ensures the stable operation of the SICs in the low-temperature operating environment. The ionic conductivity at different temperatures was characterized by electrochemical impedance spectroscopy (EIS) (Figure S2). The ionic conductivity of NaT, NaD, and NaG decreases significantly with decreasing temperature. The TE electrolyte exhibits an ionic conductivity of 2.34 $mS{\cdot}cm^{-1}$, which far exceeds ionic conductivities of 0.948 $mS{\cdot}cm^{-1}$ (NaT), 0.146 $mS{\cdot}cm^{-1}$ (NaD), 0.496 $mS{\cdot}cm^{-1}$ (NaG) and 0.054 $mS{\cdot}cm^{-1}$ for the commercialized electrolyte EC/DEC (Figures 1(e) and (f)) at −40 °C. The ion transport activation energy (ΔE) can be obtained by mathematically fitting the ion conductivity and temperature. The ion transport activation energy of TE electrolyte is 0.228 eV, lower than the activation energy of the single-ether electrolytes of 0.382 eV (NaT), 0.524 eV (NaD), and 0.90 eV (NaG) (Figure 1(g)). This implies better ionic kinetics of Na^+ in TE electrolytes in low-temperature operating environments. In contrast, the ionic conductivity of the commercial electrolyte decreases abruptly at −30 °C, even it cannot be fitted to the activation energy (Figure S3).

The Na^+ solvation structure is directly related to the Na^+ ion transport dynamics of the SIC. To better understand the effect of solvent diversity in solvated sheaths on Na^+ transport dynamics, the electrolyte with different solvents was simulated with classical molecular dynamics (MD). In Figures 2(a) and S3, the radial distribution function of Na^+ in TE electrolyte and single-ether electrolyte all showed a typical contact ion pair (CIP) structure[33]. Remarkably, MD simulations unveil a distinctive solvation configuration in the TE electrolyte, with each Na^+ coordinated by 2.9 THF, 0.5 DME, 0.5 DIG molecules, and 0.78 PF_{6-} anions, demonstrating effective multi-ether participation. Furthermore, the Na^+ solvated sheath in the TE electrolyte did not change significantly at −40 °C (Figure 2(b)), it is suggesting that Na^+ could have room temperature-like desolvation behavior in TE electrolytes in low-temperature environment. Owing to this unique solvation structure, TE electrolyte has minimal desolvation energy compared to single-ether electrolytes at room temperature and −40 °C (Figure 2(c)), this allows the Na^+ more easily desolvation, which implies that the TE electrolyte can enhance the ionic kinetics of Na^+ and provide better performance in low-temperature operating environment.

Fourier transform infrared (FT-IR) spectroscopy further revealed the unique solvated structure in 1 M $NaPF_6$-TE electrolyte (Figure 2(d)). In this case, the free THF solvent has a characteristic peak at 908 cm^{-1} assigned to the C-O-C stretching vibration. The free DIG and DME solvents each have a characteristic peak near 1 103 cm^{-1} characterizing the C-O-C stretching vibration. The peak intensity of the free solvents was significantly lower compared to the pure solvent, indicating that more solvent was involved in the Na^+ solvated sheath. Due to the coordination of Na^+ with the solvent, the characteristic peaks of coordination with Na^+ appeared at 1 056 cm^{-1} (THF), 1 081 cm^{-1} (DME), and 1 079 cm^{-1} (DIG) in the single-ether electrolyte. A wide bulge peak appeared between 1 093 cm^{-1}–1 043 cm^{-1} in TE electrolyte, suggesting three ether-based solvents are coordinated to Na^+, which are all involved in the solvated sheath. Raman spectra of 1 M $NaPF_6$-TE electrolyte shows similar results (Figure 2(e)). The peaks at 910 cm^{-1}, 860 $cm^{-1,}$ and 850 cm^{-1} were assigned to the coordination characteristic peaks of Na^+-THF, Na^+-DME, and Na^+-DIG, respectively. indicating the THF, DME, and DIG are all coordinated to Na^+. The intensity of the Na^+-solvent coordination peak of the TE electrolyte was significantly lower than the single-ether electrolyte, indicating that the coordination capacity of Na^+ with the solvent was weakened and the desolvation energy was reduced, and Na^+ was more easily desolvated. In addition, the solvated structure of Na^+ was fitted from the range of 720 cm^{-1}–760 cm^{-1} in Raman spectra (Figures 2(f) and S5). Notably, the ratio of CIP was up to 73.2% in the TE electrolyte, higher than NaT (46.9%), NaD (62.6%) and NaG (59.9%). Furthermore, the ratio of SSIP only was 7.7% in the TE electrolyte, far lower than single-ether solvent electrolyte of 29.5% (NaT), 19.4% (NaD), and 24.5% (NaG). MD simulations showed the similar results (Figures 2(g) and S6). The higher CIP and lower

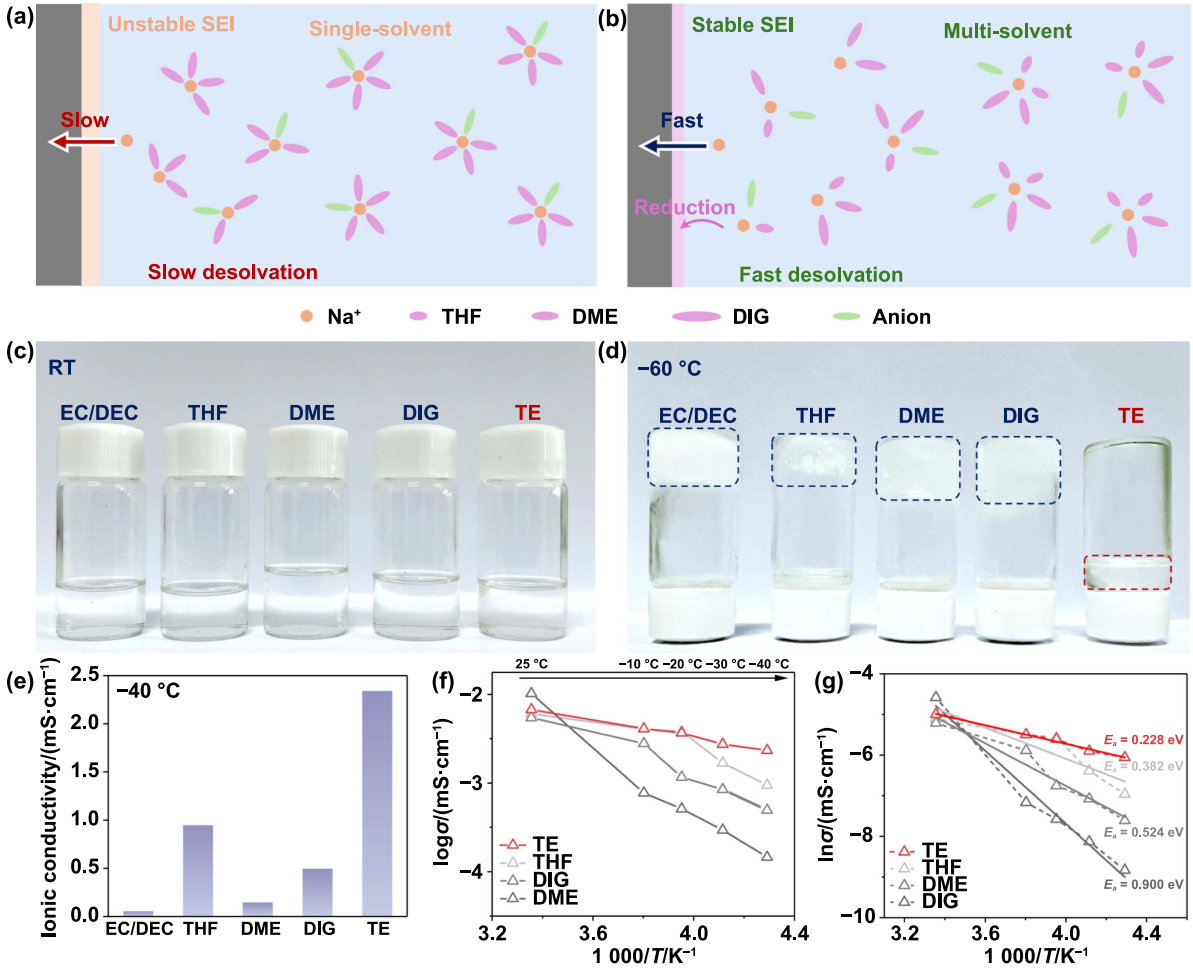

Figure 1. The Na^+ transport behavior in (a) single-solvent and (b) multi-solvent electrolytes, the digital photographs of each electrolyte placed in (c) room temperature and (d) −60 °C environments. (e) The ionic conductivity of each electrolyte at −40 °C. (f) The ionic conductivity of each electrolyte at different temperature. (g) The activation energy of each electrolyte fitting by the Arrhenius equation.

SSIP structure would make Na^+ desolvation easier and, more importantly, facilitate the formation inorganic-rich SEI[34].

The composition of the SEI has significant influence on the ionic dynamics of Na^+ and the electrochemical performance of SICs (Figures 3(a) and (b)). The composition and distribution of SEI on the HC surface were investigated using x-ray photoelectron spectroscopy (XPS) (Figure S7). The depth-dependent elemental composition profiles presented in Figure 3(c) reveal distinct distribution patterns during sputtering. Notably, the F 1s signal maintains a consistently low concentration (<3%) throughout the sputtering process. A clear inverse correlation emerges between carbon and oxygen/sodium constituents: the C 1s concentration exhibits a significant reduction with prolonged sputtering time, whereas the O 1s and Na 1s concentrations demonstrate progressive enrichment. This indicates the formation of Na_2O-rich SEI. The formation of Na_2O-rich SEI is evidenced by the characteristic peaks of Na_2O (~530.2 eV) in the O1s spectra (Figure 3(e)), and the characteristic peak intensity increases gradually with increasing sputtering time, indicating that the Na_2O content of the SEI increases gradually from outside to inside, which is consistent with the curve of the elemental ratio of the O 1s.

To further investigate the structure and composition of SEI, we assembled a Na | TE | Cu cell. The Na-Cu cell was able to form SEI when Na was deposited on the surface of Cu foil, while the composition and structure of SEI were characterized by transmission electron microscopy (TEM). TEM image (Figure S8(a)) shows that the inorganic components in SEI are mainly Na_2O (lattice streaks in yellow circles) and Na_2CO_3 (lattice streaks in orange circles), where Na_2O is the main component of SEI. Polycrystalline diffraction rings of Figure S8(a) formed by fast Fourier transformation (FFT) (Figure S8(b)) demonstrate the presence of only Na_2O and Na_2CO_3 in SEI, while no lattice streaks of NaF are found. The Na_2O-rich SEI structure matches the results of the XPS test. Surprisingly, in previous studies, SEI derived from solvent molecular usually contains a large amount of organic sodium salts. The organic sodium salt-rich SEI dissolves easily during cycling, leading to significant reduction in SIC lifespan. Compared to organic sodium salts, inorganic sodium salts are thinner and more stable[35]. To obtain inorganic SEI, the general strategy is to construct anion-dominated solvated structures (CIP or AGG) to form inorganic sodium salt-rich SEI structure (the majority of NaF)[36]. However, by constructing

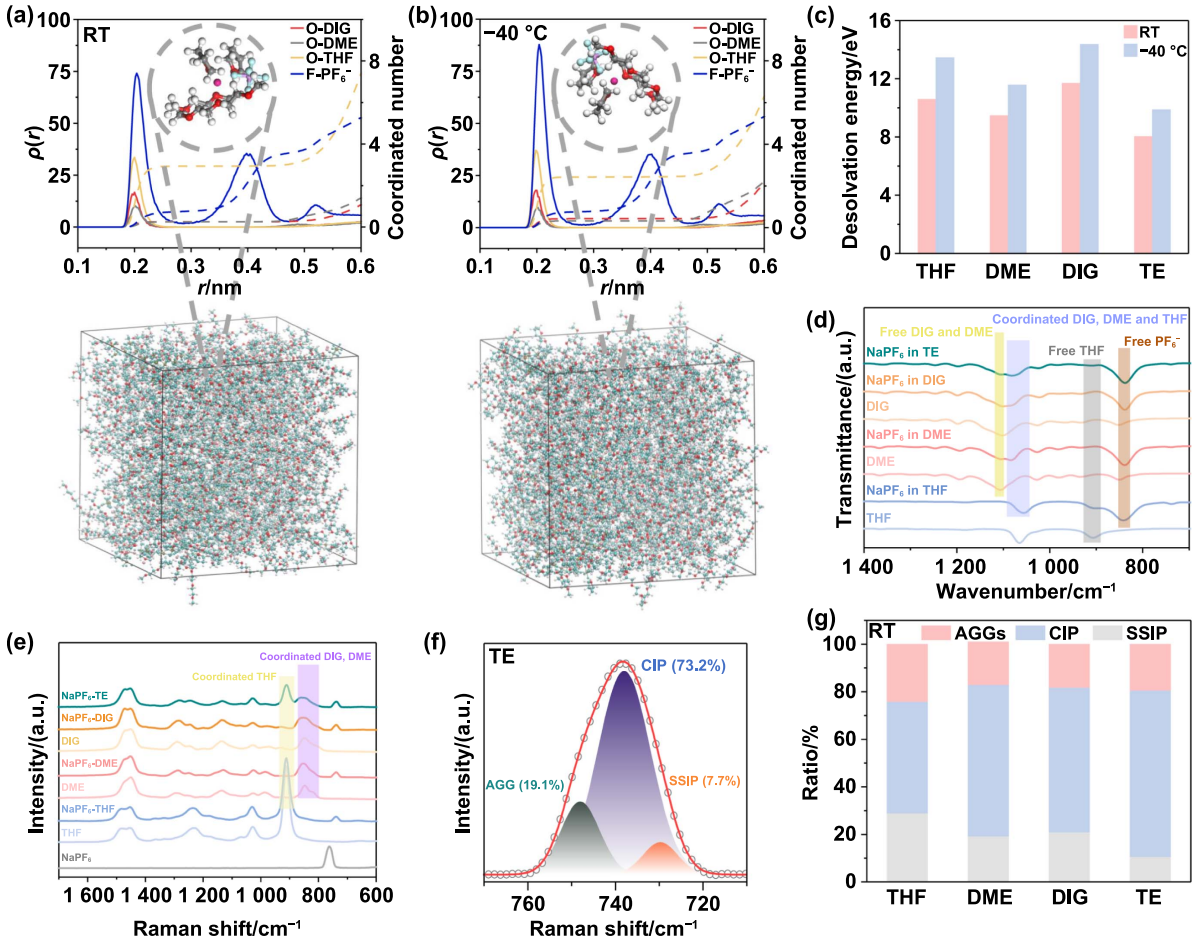

Figure 2. The Na^+ radial distribution functions of 1 M $NaPF_6$-TE at (a) room temperature and (b) −40 °C, and the inner picture is the snapshot of solvation structure (below picture) extracted from MD simulation of 1 M $NaPF_6$-TE electrolyte at room temperature. (c) The desolvation energy of different ether-based electrolyte at room temperature and −40 °C, (d) the FT-IR spectra and (e) Raman spectra of $NaPF_6$, solvent, single-ether electrolyte, and 1 M $NaPF_6$-TE electrolyte. (f) The fitted SSIP, CIP, and AGG solvation structure collected from Raman spectra of 1 M $NaPF_6$-TE electrolyte at room temperature, (g) the ratio of solvated structures (SSIP, CIP, and AGG) of different ether-based electrolyte at room temperature based on MD simulation.

a solvation sheath with multi-ether solvents, the anion-derived SEI is transformed into an inorganic Na_2O-rich SEI derived from ether-based solvents. The Na^+ transport energy barriers in NaF and Na_2O were calculated (Figure S9). The results showed that the Na^+ transport energy barrier in Na_2O was smaller than NaF, indicating that the Na_2O-rich SEI was more favorable for rapid Na^+ transport and enhanced the Na^+ ionic kinetics. Therefore, we adopt multi-ether solvent modulation strategy to modulate Na^+ solvation structure, successfully promoting the desolvation of Na^+, and construct Na_2O-rich SEI favor to fast ion transport. It provides a powerful support for the fast transport of Na^+, especially in low-temperature operating environments.

The electrochemical performance of SICs is controlled by the HC anode kinetics due to the difference between the anode and cathode kinetics of SICs[37]. In order to comprehensively evaluate the impact of multi-solvent modulation solvation sheath strategy on the electrochemical performance of SIC, the electrochemical performance of HC anode in 1 M $NaPF_6$-TE electrolyte was first characterized. The HC anode in 1 M $NaPF_6$-TE electrolyte exhibited impressive specific capacities of 420, 393, 384, 372, 353, 335 $mAh{\cdot}g^{-1}$ obtained at 0.05, 0.1, 0.2, 0.5, 1 and 2 $A{\cdot}g^{-1}$ in room temperature environment, respectively (Figure 4(a)). Rate performance is superior to commercial electrolytes EC/DEC and single-ether electrolytes (Figure 4(b)). It is attributed to the fast Na^+ ionic kinetics in the 1 M $NaPF_6$-TE electrolyte. The Na^+ ionic dynamics in the 1 M $NaPF_6$-TE electrolyte were further revealed using electrochemical impedance spectroscopy (EIS) (Figures 4(c) and S10). We fitted the EIS curves based on the equivalent circuit (Figure S11). Benefiting from the Na_2O-rich SEI with lower transport barrier, the impedance of the SEI (R_{SEI}) in 1 M $NaPF_6$-TE electrolyte is 0.4 Ω, which is lower than that of commercial electrolytes EC/DEC with 88 Ω, and single-solvent electrolytes with 1.1 Ω (THF), 0.7 Ω (DME), and 1.7 Ω (DIG) (Figure 4(d)). To evaluate the stability of HC anode in TE electrolyte, the cycle performance of HC was tested in 1 M $NaPF_6$-TE. The HC anode can maintain 95% specific capacity after 200 charge/discharge cycles at 0.1 $A{\cdot}g^{-1}$, demonstrating excellent cycle stability (Figure 4(e)). It could attribute to

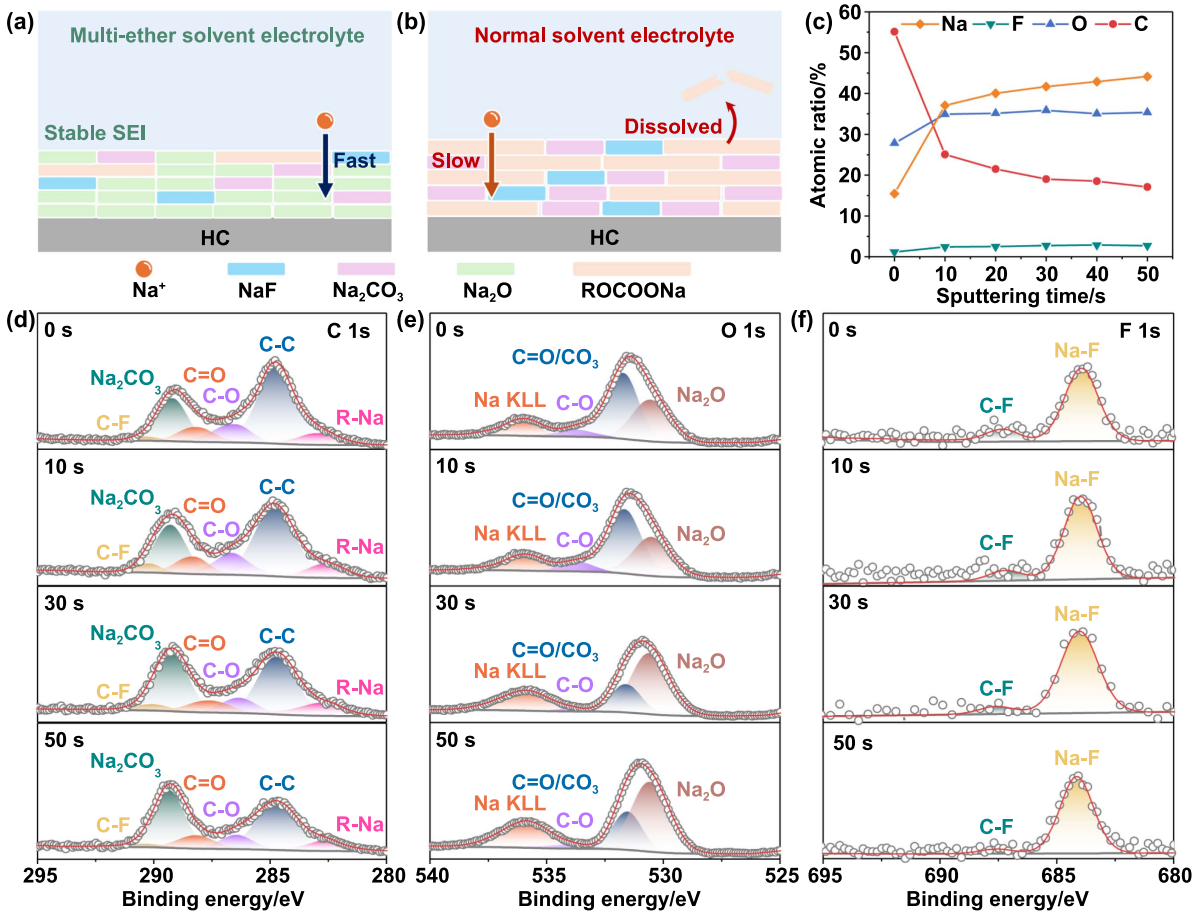

Figure 3. The schematic of SEI formed in (a) multi-ether solvent electrolyte and (b) normal solvent electrolyte, (c) the plot of the variation of atomic ratio of different elements with increasing etch depth, the fitted peaks of (d) C 1s, (e) O 1s and (f) F 1s at different sputtering times in XPS spectra.

the lower desolvation energy of Na^+ in the 1 M $NaPF_6$-TE electrolyte, which avoids the co-insertion of Na^+ and solvent molecules. Meanwhile, the stable Na_2O-rich SEI avoids electrolyte loss from SEI dissolution, and the low R_{SEI} ensures rapid Na^+ transport in the SEI. For evaluating the applicability of 1 M $NaPF_6$-TE electrolyte in high-altitude cold regions, the electrochemical performance of half-cells assembled with 1 M $NaPF_6$-TE electrolyte was tested at −40 °C. The HC anode exhibited an ultra-high specific capacity of 331 mAh·g^{-1} at 0.05 A·g^{-1} at −40 °C, far higher than the commercial electrolytes EC/DEC of 11 mAh·g^{-1} and single-ether electrolytes of 258 mAh·g^{-1} (THF), 112 mAh·g^{-1} (DME) and 82 mAh·g^{-1} (DIG) (Figure 4(f)). Due to the unique solvated structure, the rate performance of HC in TE electrolyte is much better than EC-based electrolyte and single-ether electrolytes at −40 °C (Figure 4(g)). In addition, the HC anode shows excellent specific capacity of 325, 314, 298, 270, and 200 mAh·g^{-1} at 0.1, 0.2, 0.5, 1 and 2 A·g^{-1}current densities, respectively, demonstrating impressive low-temperature rate performance (Figures 4(h) and S12). The kinetic behavior of Na^+ at −40 °C operating environment was studied by EIS (Figure S13(a)). The HC anode in TE electrolyte exhibited very low R_{SEI} (4.9 Ω) and R_{ct} (4.6 Ω) at −40 °C, demonstrating excellent low-temperature ionic dynamics. In contrast, commercial EC-based electrolyte and single-ether electrolytes showed a sharp impedance increase at −40 °C (Figures S13(b) and (c)), indicating the slow ionic dynamics of Na^+. This leads to their poor rate performance at at −40 °C, consistent with the test results in Figure 4(g).

For evaluating the application of 1 M $NaPF_6$-TE electrolyte in devices, sodium ion hybrid capacitors (HC||AC) were assembled using activated carbon as the cathode, as shown in Figure 5(a). Before the SICs were assembled, the electrochemical performance of the AC cathode in the 1 M $NaPF_6$-TE electrolyte needed to be characterized at first. The AC cathode shows approximately rectangular cyclic voltammetry (CV) curves (Figure S14), indicating AC cathode follows the typical electronic double layer (EDL) mechanism. In addition, the AC cathode has excellent rate performance (Figure S15). The specific capacity of 74 mAh·g^{-1} at 10 A·g^{-1} current density provides up to 86% capacity retention compared to the capacity at 0.05 A·g^{-1} current density (86 mAh·g^{-1}). Outstanding rate performance indicates that the 1 M $NaPF_6$-TE electrolyte is well-compatible with the AC cathode. Meanwhile, the higher specific capacity can better cooperate with the capacity of HC anode, so that the SIC can obtain better electrochemical

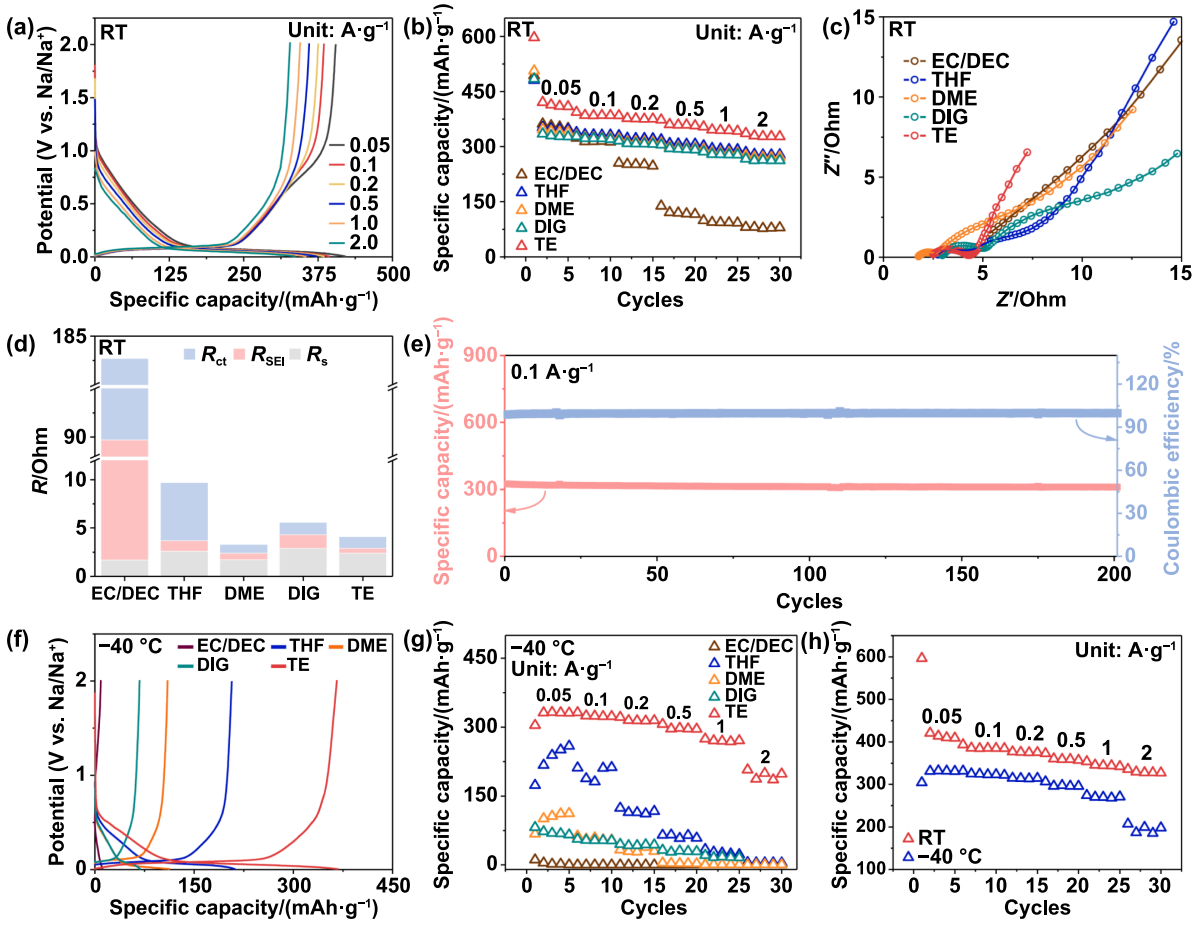

Figure 4. The electrochemical characterization of HC anodes. (a) The galvanostatic charge-discharge of HC in 1 M $NaPF_6$-TE electrolyte at room temperature. (b) The rate performance of different electrolytes at room temperature. (c) The Nyquist plot of HC anode in different electrolytes at room temperature. (d) The fitted R_s, R_{SEI} and R_{ct} of HC anode in different electrolytes. (e) The cycling performance and coulombic efficiency of HC anode at 0.1 $A{\cdot}g^{-1}$ at room temperature. (f) The specific capacity of HC anode using different electrolytes at 0.1 $A{\cdot}g^{-1}$ in −40 °C. (g) The rate performance of HC anode in different electrolytes at −40 °C. (h) The rate performance of HC anode in 1 M $NaPF_6$-TE electrolyte at room temperature and −40 °C.

performance. The cycling stability of the AC cathode was systematically evaluated under a constant current density of 1 $A{\cdot}g^{-1}$. As demonstrated in Figure S16, the electrode exhibited excellent capacity retention with 80% of its initial capacity preserved after 1 000 continuous charge/discharge cycles. Linear sweep voltammetry (LSV) measurements showed that the 1 M $NaPF_6$-TE electrolyte achieved high anodic stability of 4.20 V (Figure S17), implying SIC potential usability at high voltage. The HC was pre-sodiation firstly before the SIC assembling, which could minimize the capacity loss caused by the electrolyte depletion. SIC was assembled by combining HC and AC in a 1: 2 active substance mass ratio. Figure 5(b) shows the CV curves of the HC anode and AC cathode at 1 $mV{\cdot}s^{-1}$, revealing the combined energy storage mechanisms of the Faradaic and EDL processes. The galvanostatic charge-discharge (GCD) curves show typical capacitive features (Figure 5(c)), demonstrating the SIC is mainly controlled by the EDL mechanism. The SIC shows excellent rate performance with specific capacities of 79, 62, 54, 50, 48, 45, 39, and 34 $mAh{\cdot}g^{-1}$ at 0.05, 0.1, 0.2, 0.5, 1, 2, 5, and 10 $A{\cdot}g^{-1}$, respectively, in the room-temperature environment. It is attributed to the well matching of kinetics and capacity between HC anode and AC cathode in the 1 M $NaPF_6$-TE electrolyte. In addition, the cycling stability of the SIC was evaluated in room-temperature environment. The SIC shows excellent cycling stability with a capacity retention of 96% after cycling 2 000 cycles at 2 $A{\cdot}g^{-1}$ current density (Figures 5(d) and S18). When the voltage window was set to 1 V − 3.7 V, the capacity retention of SIC was 80% after 9 000 cycles at 5 $A{\cdot}g^{-1}$ (Figures S19 and S20).

To evaluate the applicability of the SICs in extreme environments, the SICs electrochemical performance was tested in low-temperature operating environment. Compared to the specific capacity at 0.1 $A{\cdot}g^{-1}$ at room temperature, the capacity retention at −20 °C and −40 °C is 73% (45 $mAh{\cdot}g^{-1}$) and 64% (40 $mAh{\cdot}g^{-1}$) (Figure 5(e)), respectively, demonstrating excellent low-temperature rate performance. In addition, the SIC maintains specific capacity of 15 $mAh{\cdot}g^{-1}$ at 10 $A{\cdot}g^{-1}$ current density at −40 °C operating environment, which is the best performance of the SIC in −40 °C operating environment

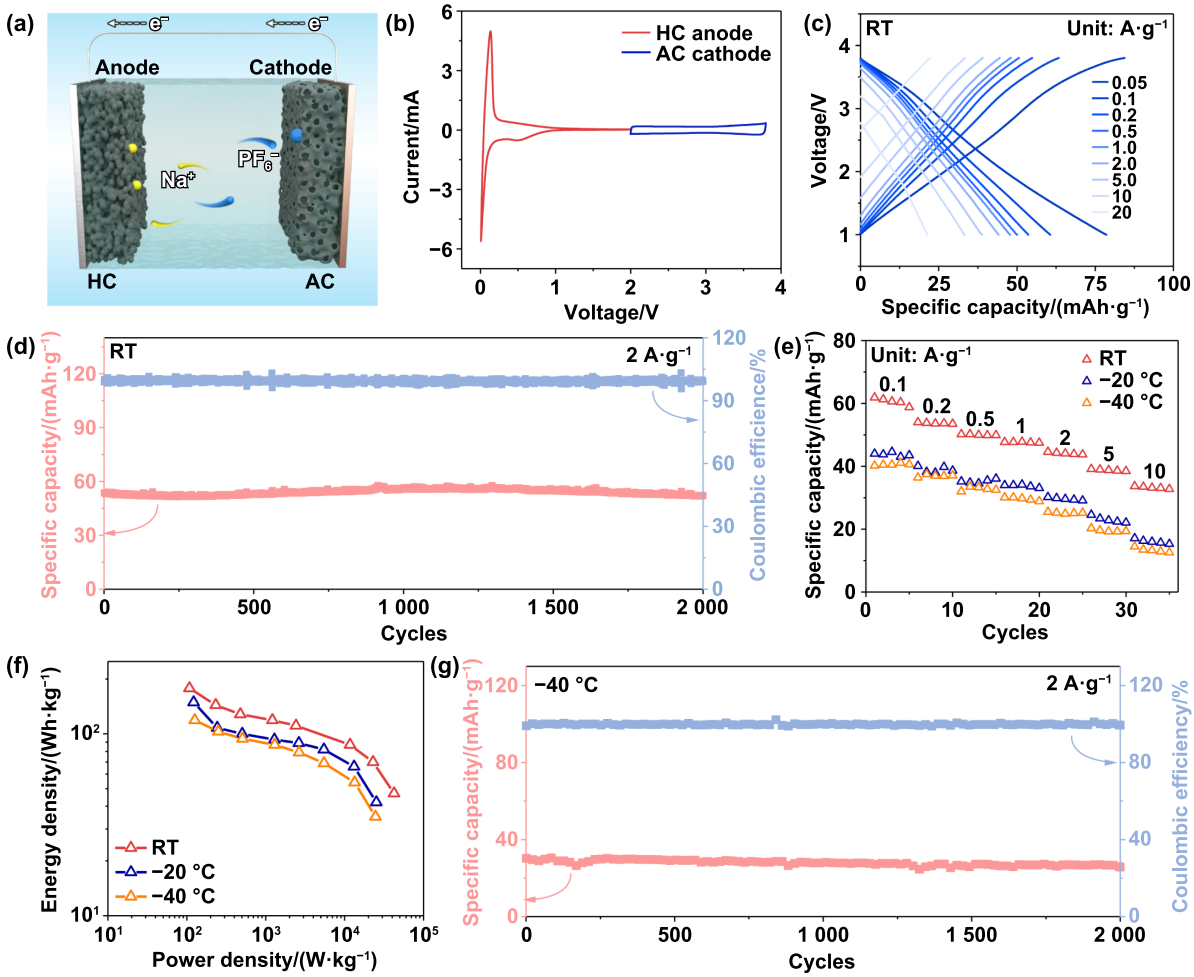

Figure 5. The electrochemical characterization of SIC. (a) The operating principal schematic of SIC, (b) CV curves of HC anode (left) and AC cathode (right), (c) the galvanostatic charge-discharge of SIC at different current densities at room temperature. (d) The cycling performance of SIC at 2 $A{\cdot}g^{-1}$ at room temperature, (e) the rate performance of SIC at room temperature, −20 °C and −40 °C. (f) The ragone plot of SIC at room temperature, −20 °C and −40 °C. (g) The cycling performance of SIC at 2 $A{\cdot}g^{-1}$ in −40 °C.

until now. The Ragone plot shows the energy density of the SIC at different power densities as shown in Figure 5(f). The SIC achieves the energy density of 178 $Wh{\cdot}kg^{-1}$ at a power density of 109 $W{\cdot}kg^{-1}$ in room temperature environment. The energy density can reach 70 $Wh{\cdot}kg^{-1}$ at a power density of 22 909 $W{\cdot}kg^{-1}$ and even maintains a high energy density of 47 $Wh{\cdot}kg^{-1}$ at a power density of 42 390 $W{\cdot}kg^{-1}$. More importantly, the SIC shows impressive energy density in low-temperature operating environment. The SIC shows excellent energy densities of 149 $Wh{\cdot}kg^{-1}$ (122 $W{\cdot}kg^{-1}$) and 119 $Wh{\cdot}kg^{-1}$ (126 $W{\cdot}kg^{-1}$) in −20 °C and −40 °C operating environments, respectively. Even at high power densities of 25 200 $W{\cdot}kg^{-1}$ and 24 591 $W{\cdot}kg^{-1}$, the SIC maintains impressive energy densities of 42 $Wh{\cdot}kg^{-1}$ and 35 $Wh{\cdot}kg^{-1}$ at −20 °C and −40 °C, respectively. To our knowledge, this is the best performance of the SICs in low-temperature operating environments so far. More significantly, these performances approach or even exceed the reported literature of lithium-ion capacitors (LICs) (Figure S21). Furthermore, the stability of the SIC in a low-temperature operating environment was evaluated (Figures 5(g) and S22). The capacity retention was 84% after 2 000 cycles at 2 $A{\cdot}g^{-1}$ current density at −40 °C. Furthermore, the SIC was still functional after 9 000 cycles and provides a specific capacity of 9 $mAh{\cdot}g^{-1}$ (Figure S23). All of the above excellent performances demonstrate that the SIC based on 1 M $NaPF_6$-TE electrolyte is an ideal energy storage device in low-temperature operating environments.

In conclusion, we propose a new electrolyte design strategy and successfully realize a SIC combined of high energy density and high power density running stably in a low-temperature operating environment. Introducing a variety of ether-based solvent molecules into the Na^+ solvation sheath reduces the desolvation energy of Na^+. More importantly, the unique Na^+ solvation structure derives Na_2O-rich inorganic SEI, which ensures fast ionic kinetics of Na^+ in different temperature operating environments. The HC anode maintains high specific capacity of 331 $mAh{\cdot}g^{-1}$ (0.05 $A{\cdot}g^{-1}$) and 200 $mAh{\cdot}g^{-1}$ (2 $A{\cdot}g^{-1}$) at −40 °C. The assembled SIC achieves an ultra-high energy density of 119 $Wh{\cdot}kg^{-1}$ (power density of 126 $W{\cdot}kg^{-1}$) and an impressive power density of

24 591 $W{\cdot}kg^{-1}$ (energy density of 35 $Wh{\cdot}kg^{-1}$) at −40 °C. This work provides a new design strategy for the development of high performance SICs for low-temperature operating.

Acknowledgments

The authors acknowledge the support from National Outstanding Youth Science Fund (52222314), Near Space Technology and Industry Guidance Fund Project (LKJJ-2023010-01), CNPC Innovation Found (2021DQ02-1001), Dalian Outstanding Youth Science and Technology Talent Project (2023RJ006), Dalian Science and Technology Innovation Project (2022JJ12GX022), Xinghai Talent Cultivation Plan (X20200303).

ORCID iD

Fangyuan Hu https://orcid.org/0000-0002-1611-7372

References

[1] Bonaccorso F, Colombo L, Yu G H, Stoller M, Tozzini V, Ferrari A C, Ruoff R S and Pellegrini V. 2015. Graphene, related two-dimensional crystals, and hybrid systems for energy conversion and storage. *Science* **347**, 1246501.
[2] Xu Z and Wang J. 2022. Toward emerging sodium-based energy storage technologies: from performance to sustainability. *Adv. Energy Mater.* **12**, 2201692.
[3] Pei M F, Liu D M, Jin X, Li B R, Jiang W Y, Song Z H, Jian X G and Hu F Y. 2024. Na_2S *in-situ* infiltrated in actived carbon as high-efficiency presodiation additives for sodium ion hybrid capacitors. *Carbon Neutral.* **3**, 461–470.
[4] Liu S Y, Cheng H T, Mao R Y, Jiang W Y, Wang L, Song Z H, Pei M F, Zhang T P and Hu F Y. 2023. Designing zwitterionic gel polymer electrolytes with dual-ion solvation regulation enabling stable sodium ion capacitor. *Adv. Energy Mater.* **13**, 2300068.
[5] Zhao Y H, Li N, Xie K Y, Wang C, Zhou S S, Zhang X G and Ye C. 2025. Manufacturing of lithium battery toward deep-sea environment. *Int. J. Extrem. Manuf.* **7**, 022009.
[6] Wang F, Jiang Z M, Zhang Y Y, Zhang Y L, Li J D, Wang H B, Jiang Y Z, Xing G C, Liu H C and Tang Y X. 2024. Revitalizing sodium-ion batteries via controllable microstructures and advanced electrolytes for hard carbon. *eScience* **4**, 100181.
[7] Larcher D and Tarascon J M. 2015. Towards greener and more sustainable batteries for electrical energy storage. *Nat. Chem.* **7**, 19–29.
[8] Liu S Y, Hu F Y, Shao W L, Zhang W S, Zhang T P, Song C, Yao M, Huang H and Jian X G. 2020. A novel strategy of *in situ* trimerization of cyano groups between the $Ti_3C_2T_x$ (MXene) interlayers for high-energy and high-power sodium-ion capacitors. *Nano-Micro Lett.* **12**, 135.
[9] Yang B J, Chen J T, Lei S L, Guo R S, Li H X, Shi S Q and Yan X B. 2018. Spontaneous growth of 3D framework carbon from sodium citrate for high energy-and power-density and long-life sodium-ion hybrid capacitors. *Adv. Energy Mater.* **8**, 1702409.
[10] Ding J, Hu W B, Paek E and Mitlin D. 2018. Review of hybrid ion capacitors: from aqueous to lithium to sodium. *Chem. Rev.* **118**, 6457–6498.
[11] Lu Z Y, Yang H J, Guo Y, Lin H X, Shan P Z, Wu S C, He P, Yang Y, Yang Q H and Zhou H S. 2024. Consummating ion desolvation in hard carbon anodes for reversible sodium storage. *Nat. Commun.* **15**, 3497.
[12] Liu M Q, Wang Y H, Wu F, Bai Y, Li Y, Gong Y T, Feng X, Li Y, Wang X R and Wu C. 2022. Advances in carbon materials for sodium and potassium storage. *Adv. Funct. Mater.* **32**, 2203117.
[13] Chen J W, Peng Y, Yin Y, Fang Z, Cao Y J, Wang Y G, Dong X L and Xia Y Y. 2021. A desolvation-free sodium dual-ion chemistry for high power density and extremely low temperature. *Angew. Chem., Int. Ed.* **60**, 23858–23862.
[14] Wu Z X, Huang Z D, Zhang R, Hou Y and Zhi C Y. 2024. Aqueous electrolyte additives for zinc-ion batteries. *Int. J. Extrem. Manuf.* **6**, 062002.
[15] Gupta A and Manthiram A. 2020. Designing advanced lithium-based batteries for low-temperature conditions. *Adv. Energy Mater.* **10**, 2001972.
[16] Wang S Z, Zhang X G, Gu Y, Tang S and Fu Y Z. 2024. An ultrastable low-temperature Na metal battery enabled by synergy between weakly solvating solvents. *J. Am. Chem. Soc.* **146**, 3854–3860.
[17] Zheng X Y, Huang L Q, Ye X L, Zhang J X, Min F Y, Luo W and Huang Y H. 2021. Critical effects of electrolyte recipes for Li and Na metal batteries. *Chem* **7**, 2312–2346.
[18] Zhong S E et al. 2023. Molecular engineering on solvation structure of carbonate electrolyte toward durable sodium metal battery at −40 °C. *Angew. Chem., Int. Ed.* **135**, e202301169.
[19] Wang C L, Thenuwara A C, Luo J M, Shetty P P, McDowell M T, Zhu H Y, Posada-Pérez S, Xiong H, Hautier G and Li W Y. 2022. Extending the low-temperature operation of sodium metal batteries combining linear and cyclic ether-based electrolyte solutions. *Nat. Commun.* **13**, 4934.
[20] Fang H Y, Huang Y H, Hu W, Song Z H, Wei X S, Geng J R, Jiang Z L, Qu H, Chen J and Li F J. 2024. Regulating ion-dipole interactions in weakly solvating electrolyte towards ultra-low temperature sodium-ion batteries. *Angew. Chem., Int. Ed.* **63**, e202400539.
[21] Xia Y, Yu F D, Nie D, Jiang Y S, Sun M Y, Que L F, Deng L, Zhao L, Zhang Q Y and Wang Z B. 2024. Unlocking fast potassium ion kinetics: high-rate and long-life potassium dual-ion battery for operation at −60 °C. *Angew. Chem., Int. Ed.* **63**, e202406765.
[22] Zhou J et al. 2022. Low-temperature and high-rate sodium metal batteries enabled by electrolyte chemistry. *Energy Storage Mater.* **50**, 47–54.
[23] Yu D D et al. 2024. Low-temperature and fast-charge sodium metal batteries. *Small* **20**, 2311810.
[24] He J R, Bhargav A, Su L S, Lamb J, Okasinski J, Shin W and Manthiram A. 2024. Tuning the solvation structure with salts for stable sodium-metal batteries. *Nat. Energy* **9**, 446–456.
[25] Wang S Y et al. 2023. Unraveling the solvent effect on solid-electrolyte interphase formation for sodium metal batteries. *Angew. Chem., Int. Ed.* **135**, e202313447.
[26] Holoubek J et al. 2021. Tailoring electrolyte solvation for Li metal batteries cycled at ultra-low temperature. *Nat. Energy*. **6**, 303–313.
[27] Li Y, Wu F, Li Y, Liu M Q, Feng X, Bai Y and Wu C. 2022. Ether-based electrolytes for sodium ion batteries. *Chem. Soc Rev.* **51**, 4484–4536.
[28] Zeng H P et al. 2024. Beyond LiF: tailoring Li_2O-dominated solid electrolyte interphase for stable lithium metal batteries. *ACS Nano* **18**, 1969–1981.
[29] Huang W, Wang H S, Boyle D T, Li Y Z and Cui Y. 2020. Resolving nanoscopic and mesoscopic heterogeneity of fluorinated species in battery solid-electrolyte interphases by cryogenic electron microscopy. *ACS Energy Lett.* **5**, 1128–1135.

[30] Hobold G M, Wang C Z, Steinberg K, Li Y Z and Gallant B M. 2024. High lithium oxide prevalence in the lithium solid-electrolyte interphase for high Coulombic efficiency. *Nat. Energy* **9**, 580–591.
[31] Lowe J S and Siegel D J. 2020. Modeling the interface between lithium metal and its native oxide. *ACS Appl. Mater. Interfaces* **12**, 46015–46026.
[32] Kim S C et al. 2023. High-entropy electrolytes for practical lithium metal batteries. *Nat. Energy* **8**, 814–826.
[33] Hu Y S and Pan H L. 2022. Solvation structures in electrolyte and the interfacial chemistry for Na-Ion batteries. *ACS Energy Lett.* **7**, 4501–4503.
[34] Cheng H R et al. 2022. Emerging era of electrolyte solvation structure and interfacial model in batteries. *ACS Energy Lett.* **7**, 490–513.
[35] Liu S F et al. 2021. An inorganic-rich solid electrolyte interphase for advanced lithium-metal batteries in carbonate electrolytes. *Angew. Chem., Int. Ed.* **60**, 3661–3671.
[36] Xu J J, Koverga V, Phan A, Li A M, Zhang N, Baek M, Jayawardana C, Lucht B L, Ngo A T and Wang C S. 2024. Revealing the anion–solvent interaction for ultra-low temperature lithium metal batteries. *Adv. Mater.* **36**, 2306462.
[37] Cai P, Zou K Y, Deng X L, Wang B W, Zheng M, Li L H, Hou H S, Zou G Q and Ji X B. 2021. Comprehensive Understanding of sodium-ion capacitors: definition, mechanisms, configurations, materials, key technologies, and future developments. *Adv. Energy Mater.* **11**, 2003804.